Electrocatalysis (2017) 8:51–58
DOI 10.1007/s12678-016-0340-z

ORIGINAL RESEARCH

Pt Nanoparticles Supported on Niobium-Doped Tin Dioxide: Impact of the Support Morphology on Pt Utilization and Electrocatalytic Activity

Gwenn Cognard[1,2] · Guillaume Ozouf[3] · Christian Beauger[3] · Ignacio Jiménez-Morales[4] · Sara Cavaliere[4] · Deborah Jones[4] · Jacques Rozière[4] · Marian Chatenet[1,2,3,5] · Frédéric Maillard[1,2]

Published online: 10 November 2016

Abstract Two synthesis routes were used to design high surface area niobium-doped tin dioxide (Nb-doped SnO_2, NTO) nanostructures with either loose-tube (fibre-in-tube) morphology using electrospinning or aerogel morphology using a sol-gel process. A higher specific surface area but a lower apparent electrical conductivity was obtained on the NTO aerogel compared to the loose tubes. The NTO aerogels and loose tubes and two reference materials (undoped SnO_2 aerogel and Vulcan XC72) were platinized with a single colloidal suspension and tested as oxygen reduction reaction (ORR) electrocatalysts for proton-exchange membrane fuel cell (PEMFC) applications. The specific surface area of the supports strongly influenced the mass fraction of deposited Pt nanoparticles (NPs) and their degree of agglomeration. The apparent electrical conductivity of the supports determined the electrochemically active surface area (ECSA) and the catalytic activity of the Pt NPs for the ORR. Based on these findings, electrospinning appears to be the preferred route to synthesize NTO supports for PEMFC cathode application.

Keywords Niobium-doped tin dioxide (Nb-doped SnO_2, NTO) · Platinum · Aerogel · Loose tubes · Oxygen reduction reaction · Proton exchange membrane fuel cell

Introduction

Proton exchange membrane fuel cells (PEMFC) are efficient and promising energy converters. One of the remaining scientific hurdles to be overcome before their wide commercialization is their long-term stability, in particular that of the cathode electrocatalyst used to promote the oxygen reduction reaction (ORR). This reaction is catalysed by Pt or Pt-alloy nanoparticles (NPs) supported on a high surface area carbon (HSAC). However, both the metal NPs and the HSAC support suffer from severe corrosion during abnormal PEMFC operating conditions (start-up/shutdown or fuel starvation events), during which the cathode can reach electrochemical potential as high as 1.5 V vs. the reversible hydrogen electrode (RHE) [1–3]. The corrosion of the carbon support leads to detachment of the Pt-based NPs, collapse of the electrode structure, and ultimately degrades the electrical performance of the PEMFC [4–9].

Using metal oxide (MO_x) supports instead of HSAC is a promising option to overcome the issue of carbon support corrosion in PEMFC cathodes. Moreover, MO_x supports are characterized by strong catalyst-support interactions (SMSI) [10–20], which may be used to tune the catalytic activity of the Pt-based NPs, and provide enhanced resistance to NPs dissolution and ripening. According to Takabatake et al. [21],

Electronic supplementary material The online version of this article (doi:10.1007/s12678-016-0340-z) contains supplementary material, which is available to authorized users.

✉ Gwenn Cognard
gwenn.cognard@grenoble-inp.org

✉ Frédéric Maillard
frederic.maillard@lepmi.grenoble-inp.fr

[1] University Grenoble Alpes, LEPMI, F-38000 Grenoble, France

[2] CNRS, LEPMI, F-38000 Grenoble, France

[3] MINES ParisTech, PSL Research University PERSEE - Centre procédés, énergies renouvelables et systèmes énergétiques, CS 10207 rue Claude Daunesse, F-06904 Sophia Antipolis Cedex, France

[4] Institut Charles Gerhardt Montpellier, Agrégats Interfaces Matériaux pour l'Energie, Université de Montpellier, UMR CNRS 5253, Cedex 5, 34095 Montpellier, France

[5] French University Institute, Paris, France

SnO_2, TiO_2, Nb_2O_5, MoO_3, and Ta_2O_5 are viable MO_x supports for Pt-based NPs since they are thermodynamically stable under the operating conditions of PEMFC cathodes. In particular, SnO_2 has already demonstrated stability at electrode potentials that are typical of PEMFC cathodes [21–28]. Various SnO_2 morphologies have been developed including hollow spheres [29], nanowires [30], 3D multiscale structure [31], flower-like crystals [32], nanoclusters [33], loose tubes (LT, i.e., fiber-in-tube structure) [25], and aerogels (AG) [20, 34]. However, SnO_2 supports feature low electrical conductivity relative to HSAC and must be doped with Sb, Nb or mixed with carbon powders to be practically usable in PEMFCs [21–23, 27, 35]. As noted above, carbon being unstable under PEMFC operating conditions renders the last solution not practically viable [2–5, 9, 36–41]. Equally important for PEMFC cathode applications is the specific surface area achievable by the MO_x support. High specific surface area is required to maximize the dispersion of the Pt-based NPs and limit their agglomeration. However, increase in specific surface area may come at the expense of the electrical conductivity since it will result in larger content of grain boundaries, which act as resistances for electron transfer [42, 43]. Despite its fundamental and applied importance, the compromise between specific surface area and apparent electrical conductivity of MO_x supports remains understudied and is the focus of the present study.

Herein, two 5.0 at.% Nb-doped SnO_2 (NTO) supports with AG and LT structures were synthesized and characterized by physical, chemical, and electrochemical techniques. A single colloidal suspension served to decorate the NTO aerogel and loose tubes as well as two reference materials (undoped SnO_2 AG and Vulcan XC72) with Pt NPs. The catalytic performance of the synthesized electrocatalysts for the ORR was evaluated in model PEMFC operating conditions and discussed with regard to the morphological and physicochemical properties of the MO_x supports.

Experimental Section

Nb-doped SnO_2 aerogel (NTO-AG) and undoped-SnO_2 aerogel (TO-AG) were synthesized using a sol-gel route previously described in Ref. [34]. A solution containing nitric acid (HNO_3, Alfa Aesar, 2 N), water, and isopropanol (Acros Organics, 99.5 %) was slowly added drop-wise under magnetic stirring into a solution of tin isopropoxide (Alfa Aesar, 99 % (metals basis), 10 % *w*/*v* in isopropanol) in isopropanol (iPrOH) with a well-controlled amount of niobium precursor (Alfa Aesar, 99 % (metals basis), 10 % *w*/*v* in isopropanol/hexane (50:50)) to obtain the targeted ratio of dopant (5.0 at.% Nb). The sol-gel parameters were: HNO_3/Sn = 0.072 mol/mol, H_2O/Sn = 3.06 mol/mol, and iPrOH/Sn = 119 mol/mol. The as-formed gels were left for 48 h at room temperature and then washed three times a day for 2 days with iPrOH before being dried under CO_2 in supercritical conditions (P = 80 bars, T = 40 °C). The resulting aerogels were heat-treated in air at 600 °C for 5 h.

Nb-doped SnO_2 loose tubes (NTO-LT) were deposited by electrospinning, as reported in former works [25, 44]. Firstly, 0.93 g of $SnCl_2$ $2H_2O$ (98 %, Acros Organics) and 0.060 g of niobium (V) chloride (99.9 % min., Sigma Aldrich) were dissolved in 5.7 mL of absolute ethanol (puriss., Sigma-Aldrich). A second solution was prepared by dissolving 0.80 g of polyvinylpyrrolidone (average molecular weight ~ 1,300,000, Aldrich) in 3.1 mL of *N*,*N*-dimethylformamide (98 % min., Fluka). The two solutions were mixed and stirred overnight and then electrospun at room temperature using an applied voltage of 15 kV, a needle collector distance of 10 cm, and a flow rate of 0.30 mL h^{-1}. The as-spun fibres were calcined in air at 600 °C for 4 h with a heating rate of 5 °C min^{-1}.

Pt NPs were deposited on the supports via a modified polyol route. Firstly, a colloidal suspension of Pt NPs was obtained by heating a solution of $H_2PtCl_6{\cdot}6H_2O$ (Alfa Aesar, 99.9 %) in ethylene glycol (0.33 g_{Pt} L^{-1}) at 160 °C and pH 11 for 3 h under argon atmosphere. A controlled mass of a chosen support material (SnO_2-based or Vulcan XC72) was then added and the pH adjusted to 2.0 or 3.0 for SnO_2 or Vulcan XC72, respectively. The mixture was stirred for 12 h, filtered with a 0.22-μm membrane filter, and thoroughly rinsed with MilliQ®-grade (MQ-grade) water. Finally, the samples were heat-treated for 2 h at 60 °C in air.

Scanning electron microscopy (SEM) analyses were performed on the aerogels using a Supra 40 with Gemini column operated at 3.0 kV. The SnO_2-based powders were deposited on adhesive conducting carbon tapes. To avoid a charging effect, the oxides were coated with a 7.0-nm-thick Pt layer, using a Quorum (Q150 T). The morphology of the LT was imaged by field-emission SEM (FE-SEM) using a Hitachi S-4800 scanning electron microscope.

The electronic conductivity of the doped SnO_2 and Vulcan XC72 supports was determined from resistance measurements carried out at room temperature using an in-house conductivity cell equipped with four gold electrodes [45] and using conventional Van Der Pauw calculations [46]. The samples were analyzed as pellets prepared by pressing at 370 MPa for 10 min.

Nitrogen adsorption/desorption isotherms for the LT and AG samples were determined at −196 °C by means of a Micromeritics ASAP 2020 apparatus. The LT sample was outgassed overnight at 200 °C and the AG sample for 120 min at T = 100 °C under vacuum (<10^{-5} Torr). The specific surface area was calculated using the BET equation [47] assuming 0.162 nm^2 for the cross-sectional area of one N_2 molecule.

Bright-field scanning transmission electron microscopy (BF-STEM) images and X-ray energy-dispersive spectroscopy (X-EDS) elemental maps of the Pt/NTO, Pt/TO, and Pt/Vulcan

XC72 electrocatalysts were acquired using a JEOL 2100F microscope operated at 200 kV in scanning transmission electron microscopy (STEM) mode. The JEOL 2100F was equipped with a retractable large angle Silicon Drift Centurio detector for X-EDS elemental mapping. The quantitative analyses were performed on the Pt *M* and the Sn *L* lines using the *K*-factor provided by the JEOL software. Bright-field transmission electron microscopy (TEM) images of the synthesized materials were also obtained with a Jeol 2010 TEM (point-to-point resolution of 0.19 nm) operated at 200 kV.

Atomic absorption spectrometry measurements were performed on a PinAAcle 900F spectrometer (PerkinElmer) to measure the amount of Pt deposited on each support.

X-ray diffraction (XRD) was performed using a PANalytical X'Pert Pro MPD vertical goniometer/diffractometer equipped with a diffracted-beam monochromator using Cu (K_a mean) radiation ($\lambda = 0.15418$ nm) operating at 45 kV and 40 mA. The 2θ angle was scanned from 15 to 139° using a step size of 0.033° accumulating data for 480 s. The average crystallite size was estimated from the broadening of the Pt(111) diffraction peak using the Scherrer equation.

The electrochemical measurements were conducted in four-electrode Pyrex cells thermostated at 57 °C with the help of a thermostated bath circulator. The counter-electrode was a glassy carbon plate, and the reference, a mercury sulfate electrode (MSE, $Hg|Hg_2SO_4|$saturated K_2SO_4), was connected to the cell via a Luggin capillary. A Pt wire connected to the reference electrode was used to filter the high-frequency electrical noise. The working electrode was a rotating disk electrode (RDE) made of glassy carbon (Sigradur®) onto which an aliquot of 80 μL of an ink (composed of the studied electrocatalyst, Nafion® and MQ-grade water) was drop-cast and dried in air at 110 °C. The resulting porous RDE had a Pt loading of 60 $\mu g_{Pt}\ cm_{geo}^{-2}$. All the glassware used in this study was first cleaned by immersion in a H_2SO_4/H_2O_2 mixture and thoroughly rinsed with MQ-grade water. The 0.10 M H_2SO_4 electrolyte was prepared from MQ-grade water and H_2SO_4 (Suprapur®, Merck).

Ohmic drop compensated electrochemical characterizations were performed with an Autolab potentiostat (PGSTAT 302 N). The $I = f(E)$ curves and the catalytic activities presented are the average of values obtained on three independent electrodes. The working electrode was firstly immersed in the Ar-purged electrolyte at controlled potential $E = 0.40$ V vs. RHE and 15 cyclic voltammograms were recorded between 0.05 and 1.23 V vs. RHE at $v = 0.10\ V\ s^{-1}$. The electrolyte was then saturated with oxygen (O_2) and 5 cyclic voltammograms were recorded at $v = 5.0\ mV\ s^{-1}$ and $\omega = 1600$ rpm between 0.10 and 1.05 V vs. RHE, and the 5th cycle was used to determine the electrocatalytic activity for the ORR. Finally, the electrolyte was purged with Ar and 15 cyclic voltammograms were recorded at $v = 0.10\ V\ s^{-1}$ in the range $0.05 < E < 1.23$ V vs. RHE. The 15th cycle was used to determine the electrochemically active surface area (ECSA).

Results and Discussion

Synthesis and Characterization of the Supports

Figure 1 displays SEM images of SnO_2 (TO-AG) and the 5.0 at.% Nb-doped SnO_2 aerogels (NTO-AG) and loose tubes (NTO-LT) synthesized in this study. The AGs featured a three-dimensional network composed of spherical primary particles with size ca 10 nm. The primary particles were arranged as strings of beads and connected through a neck via grain boundaries. The LTs, of fibre-in-tube morphology, had an external diameter of 300 nm for the tubes and 100 nm inner fibre diameter, similarly to what was reported in previous studies [25, 48]. BET measurements revealed a specific surface area close to 80 and of 50 $m^2\ g^{-1}$ for the AG and LT morphologies, respectively. Moreover, since both supports were subjected to thermal annealing at 600 °C under air after synthesis, they crystallized in the rutile structure.

Despite this identical crystallographic structure, the NTO-AG and the NTO-LT supports featured different apparent electrical conductivities: $\sigma = 5.1\ 10^{-4}$ S cm^{-1} and $\sigma = 2.8\ 10^{-2}$ S cm^{-1}, respectively (Table 1). The 55-fold increase in apparent electrical conductivity is related to the larger NTO crystallite size of LT relative to AG: 9.8 vs. 6.3 nm, respectively. Indeed, according to the observations of Wang et al. [43] on ordered mesoporous TO

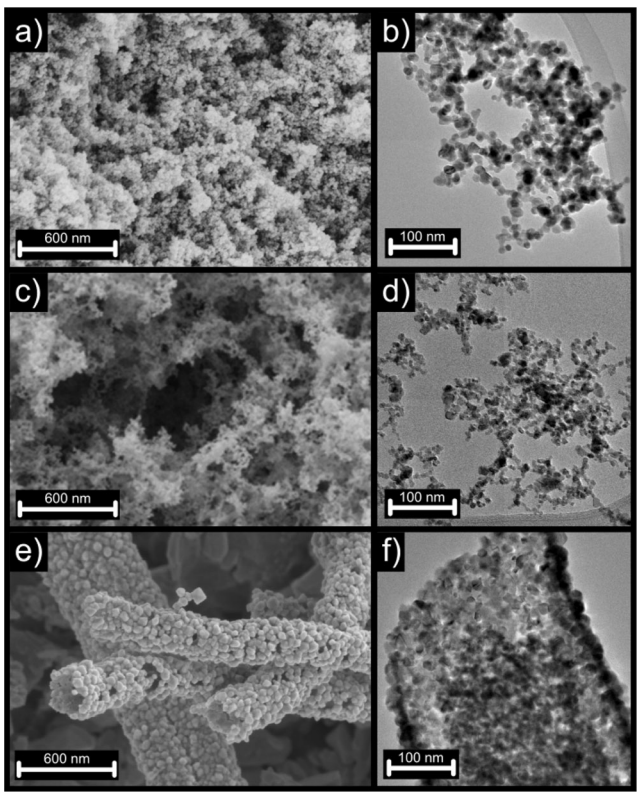

Fig. 1 SEM and TEM images of the synthesized supports: **a**, **b** SnO_2 aerogel, **c**, **d** 5.0 at.% Nb-doped SnO_2 aerogel, and **e**, **f** 5.0 at.% Nb-doped SnO_2 loose tubes

Table 1 Structural and electrical properties of the supports used in this study. The BET surface area and the pore volume for Vulcan XC72 are reprinted from Table 12.1 of Ref. [60] with permission from Wiley

	Undoped SnO_2 AG TO-AG	Nb-doped SnO_2 AG NTO-AG	Nb-doped SnO_2 LT NTO-LT	Vulcan XC72
Electrical conductivity, S cm^{-1}	–	$5.1\ 10^{-4}$	$2.8\ 10^{-2}$	5.3 [45]
BET surface area (S_{BET}), $m^2\ g^{-1}$	81	76	50	252 [60]
Total pore volume, $cm^3\ g^{-1}$	$3.1\ 10^{-1}$	$2.1\ 10^{-1}$	$1.4\ 10^{-1}$	0.63 [60]
Micropore volume, $cm^3\ g^{-1}$	$1.5\ 10^{-2}$	$1.2\ 10^{-2}$	$7.8\ 10^{-4}$	$3.7\ 10^{-2}$ [60]
Diameter of the main pores, nm	15-20-40	20-30-45	10-20-60	20-35-350
Crystallite size, nm	8.8	6.3	9.8	–

supports doped with niobium, antimony, or tantalum, small crystallite sizes favor large specific surface area but promote the formation of grain boundaries between the primary particles, which are detrimental to charge transfer.

Synthesis and Characterization of Electrocatalysts

The four MO_x supports (TO-AG, NTO-AG, NTO-LT, and Vulcan XC72) were then decorated with Pt NPs using a modified polyol route. To that goal, a single Pt colloidal suspension was used, which allowed a straightforward comparison of the catalytic performance of Pt NPs supported on carbon and doped or undoped SnO_2 supports.

As illustrated in Fig. 2, the Pt mass fraction was found to depend on the specific surface of the MO_x supports. The high specific surface area of Vulcan XC72 enabled to reach the nominal Pt mass fraction (20 wt%), while on the supports featuring lower specific surface area, less Pt NPs were deposited most likely due to the absence of anchoring sites. As revealed by atomic absorption spectroscopy (AAS) measurements, the effectively deposited Pt mass fractions were 16, 18, 12, and 20 wt% on TO-AG, NTO-AG, NTO-LT, and Vulcan XC72, respectively (the nominal Pt mass fraction was 20 wt%).

To gain further insights into the morphology of the deposited Pt NPs, BF-STEM images were combined with X-EDS elemental maps (BF-STEM and X-EDS elemental maps are

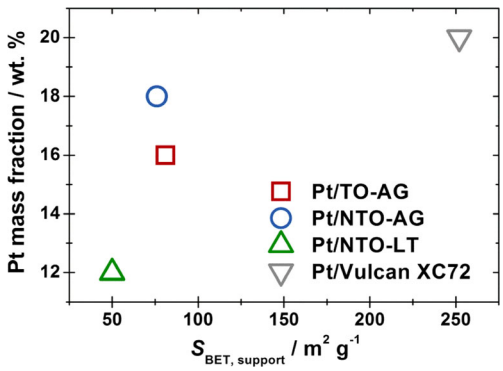

Fig. 2 Variation of the Pt mass fraction effectively deposited on the SnO_2-based supports as a function of their specific surface area

the only electron-based techniques that allow Pt NPs and SnO_2-based supports to be distinguished as both materials are crystalline and feature average *Z* values that prevent sufficient *Z*-contrast). The images revealed that the Pt NPs deposited on the TO and NTO supports were highly agglomerated (Fig. 3a, h). In contrast, the Pt NPs were well-distributed on Vulcan XC72 (Fig. 3i, j). Despite different degree of agglomeration, the mean Pt crystallite size determined from X-ray diffractograms was nearly identical for all the electrocatalysts (ca 3.5 nm, see Table 2 and Figure S1), thereby suggesting that the Pt agglomerates were indeed composed of individual nanocrystallites. This was expected, as a single Pt colloidal suspension was used to synthesize the Pt NPs on all the supports studied.

Electrochemical Characterization and ORR Activity of the Different Electrocatalysts

The electrochemical characterizations performed on the various Pt/SnO_2-based materials are presented in Fig. 4. The cyclic voltammograms (CVs) displayed in Fig. 4a unambiguously show that the utilization factor of Pt was different on different catalyst supports. Indeed, although the underpotential adsorption/desorption of hydrogen (H_{upd}) could be observed in the potential region $E < 0.40$ V vs. RHE for all electrocatalysts (Fig. 4a), the H_{upd} charge density was ca three times smaller on SnO_2-based supports relative to Vulcan XC72, translating into different Pt specific surface areas (S_{Pt}) (Fig. 4c). Note also that the formation/reduction of Pt surface oxides ($E > 0.60$ V vs. RHE) could hardly be distinguished for the SnO_2-based supports except for the most conducting Pt/NTO-LT. The charge density associated with the formation/reduction of Pt surface oxides decreased in the order Pt/Vulcan XC72 >> Pt/NTO-LT > Pt/NTO-AG >> Pt/TO-AG. The ratio of the Pt specific surface area calculated from the H_{upd} desorption charge to that calculated from the surface oxide formation (determined from the positive sweep for $0.70 < E < 1.23$ V vs. RHE) was close to 2 on Pt/Vulcan XC72, <1 on Pt/NTO-LT and Pt/NTO-AG, and nearly 0 on Pt/TO-AG. This result is easy to understand if one considers the papers of Boyle and Jones [49] and Senoo et al. [28]. These

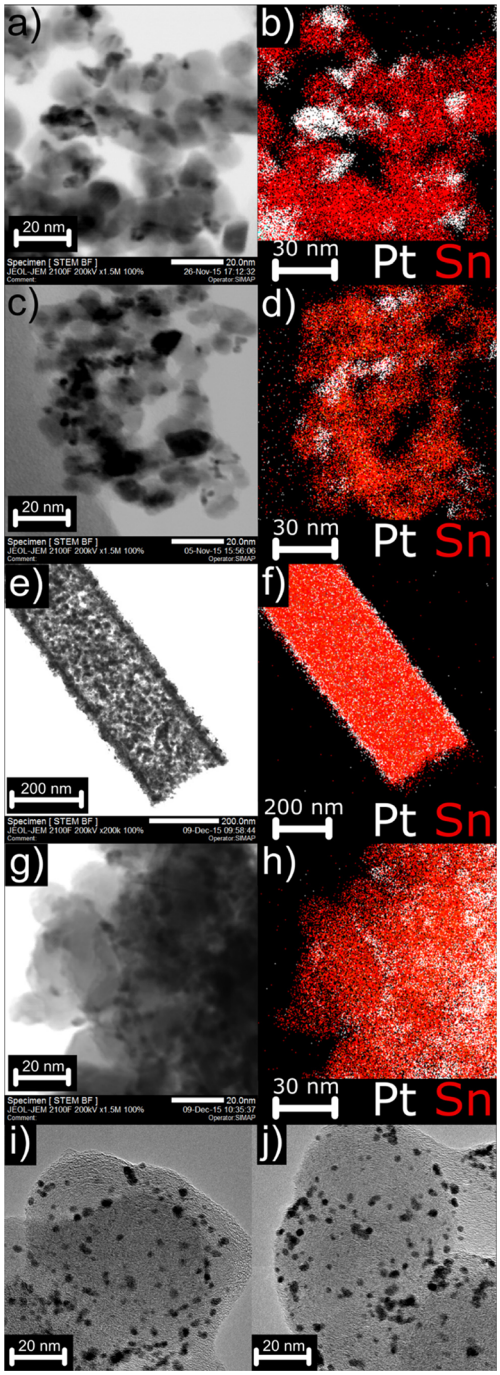

Fig. 3 STEM (**a**, **c**, **e**, **g**) and TEM (**i**, **j**) images and X-EDS elemental maps (**b**, **d**, **f**, **h**) of the synthesized electrocatalysts: (**a**, **b**) Pt/TO-AG, (c, d) Pt/NTO-AG, (**e**, **f**, **g**, **h**) Pt/NTO-LT, (**i**, **j**) Pt/Vulcan XC72

authors have shown that the chemisorption of oxygen on Nb-doped SnO_2 leads to an electron-depleted surface. This electron-depleted layer results in Pt nanoparticles being electrically disconnected in the potential region $E > 0.60$ V vs. RHE and hence results in their under-utilization.

This tendency is also visible in the linear sweep voltammograms recorded in O_2-saturated electrolyte (Fig. 4b): the absolute value of the ORR current at $E = 0.90$ V vs. RHE decreased in the sequence: Pt/Vulcan XC72 > Pt/NTO-LT > Pt/NTO-AG > Pt/TO-AG. The same holds true in the diffusion-limited region. The difference in the kinetic or the diffusion-limited region may be explained by the number of Pt active sites (electrochemically active surface area (ECSA), Pt surface coverage) or by the apparent electrical conductivities of the supports. However, since the Pt loading was constant and the Pt specific surface areas were of the same order of magnitude on the various SnO_2-based supports (Fig. 4c), the number of Pt active sites is considered to be nearly identical regardless of the support. Furthermore, the Pt coverage on the different supports (θ_{Pt}) was also nearly identical:

$$\theta_{Pt} = \frac{S_{Pt}\, m_{Pt}}{S_{support}\, m_{support}} \quad (1)$$

where S_{Pt} is the Pt-specific surface area calculated from the charge in the H_{upd} desorption region integrated between 0.05 and 0.40 V vs. RHE, m_{Pt} the mass of Pt for 1.0 g of catalyst, $S_{support}$ the specific surface area of support, and $m_{support}$ the mass of support for 1.0 g of catalyst. The θ_{Pt} values estimated from Eq. 1 are nearly identical for the four electrocatalyst: $\theta_{Pt} = 4.0$, 5.2, 4.5, and 7.0 % for 16 % Pt/TO-AG, 18 % Pt/NTO-AG, 12 % Pt/NTO-LT, and 20 % Pt/C XC72, respectively.

Hence, it can be concluded that the differences in ORR activity are mostly related to the apparent electrical conductivities of the supports. As discussed previously, the higher electrical conductivity of NTO-LT over NTO-AG is obviously related to their different crystallite sizes (Table 1). According to Xu et al. [50], the electric resistance of SnO_2-based supports is dominated by the necking between the primary particles. The authors have shown that the neck diameter (X) is proportional to the diameter of the primary particles (D) [51] and that SnO_2 becomes more resistive with a decrease of D. To evaluate the level of necking between the primary SnO_2-based particles, Senoo et al. [28] recently introduced the so-called "Necking Index (NI)." The NI is defined as the ratio of the

Table 2 Properties of the electrocatalysts synthesized in this study

	Pt/TO-AG	Pt/NTO-AG	Pt/NTO-LT	Pt/Vulcan XC72
Nominal Pt mass fraction, wt%	20	20	20	20
Measured Pt mass fraction (determined with AAS), wt%	16	18	12	20
Mean Pt crystallite size, nm	3.3	3.6	3.8	3.4

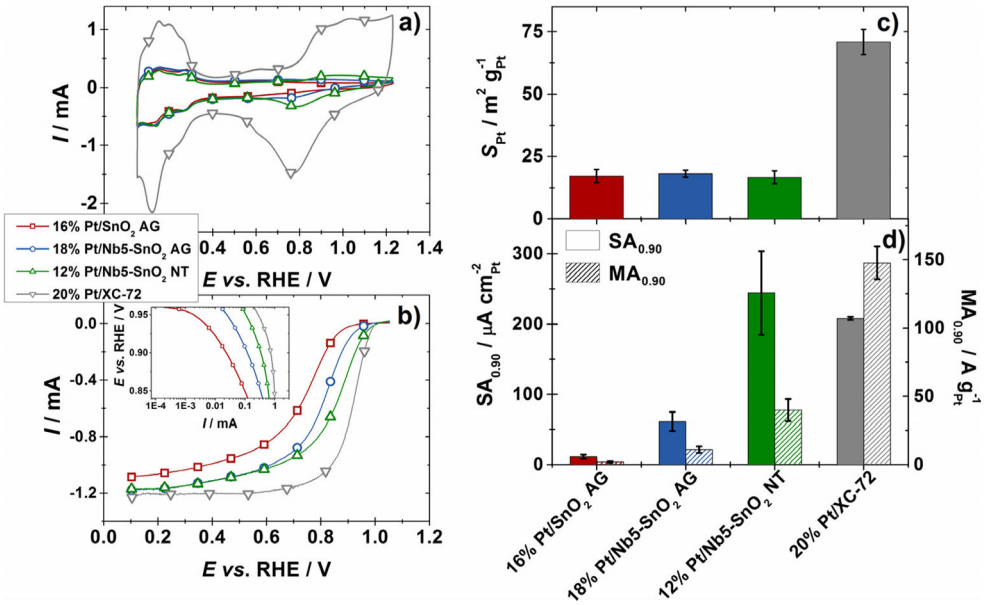

Fig. 4 Electrochemical characterization of the electrocatalysts synthesized in this study. **a** Cyclic voltammograms in Ar-purged 0.10 M H_2SO_4, **b** linear sweep voltammograms in O_2-saturated 0.10 M H_2SO_4 (inset: Tafel plot), **c** Pt specific surface area determined using the coulometry required to desorb H_{upd} from the Pt NPs, and **d** specific activity ($SA_{0.90}$) and mass activity ($MA_{0.90}$) for the ORR determined at $E = 0.90$ V vs. RHE

specific surface area determined by the BET equation to the estimated surface area assuming spherical and isolated (non-necked) SnO_2 crystallites with size determined by XRD. Hence, high NI values indicate the development of necking between SnO_2-based particles. The authors confirmed that the apparent electrical conductivity increases with decreasing the number of interconnection regions between the primary SnO_2-based particles. Similar findings by Suryamas et al. [52] on a Pt/SnO_2 nanofiber electrocatalyst and by Takasaki et al. [22] on Pt/SnO_2 and on Pt/Al-doped SnO_2 support the present conclusions: using the necking index, a decrease of the conductivity with decreasing NI values is indeed observed (Fig. 5).

Differences in surface dopant content may also account for the observed variations of the apparent electrical conductivity. Surface enrichment in doping element has already been observed in SnO_2 supports doped with Sb, Nb, or In and was found to strongly depend on both the heat-treatment and the atomic fraction of doping element [26, 53–57]. According to Cross et al. [56], beyond 4.0 at.% of Sb in a SnO_2 support, the Sb concentration at the surface is always higher than 25 at.%.

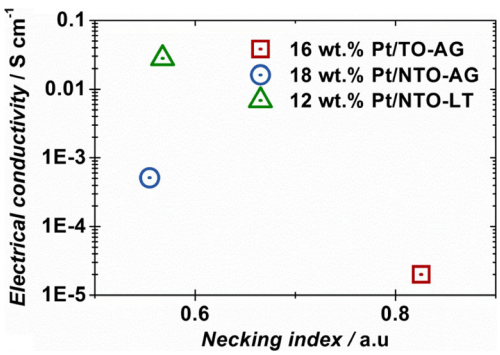

Fig. 5 Dependence of the apparent electrical conductivity of the SnO_2-based supports on the necking index

Nb surface enrichment has also been reported in a SnO_2 support doped with Nb [53]. In NTO supports, Nb surface enrichment favors the formation of micro-domains of amorphous Nb_2O_5 [58], which is an insulator (the conductivity of a Nb_2O_5 single crystal is around $\sigma = 3.0\ 10^{-6}$ S cm^{-1}) [59]. Hence, despite identical doping level (5.0 at.%), high surface area supports featuring small crystallites and thus large number of grain boundaries are likely to favor the formation of Nb_2O_5-rich domains, which will act as a barrier for the electron transfer.

Conclusion

Nb-doped SnO_2 supports are attractive alternative electrocatalyst supports to replace conventional carbon supports in PEMFC. In this study, Nb-doped or undoped SnO_2 aerogels and loose tubes were synthesized, characterized, and decorated with Pt nanoparticles using the same Pt colloidal suspension. The Pt mass fraction and the degree of dispersion of the Pt NPs were found to strongly depend on the specific surface of the support, being maximal for the supports with the higher specific surface areas. However, due to smaller crystallite size, the electrical conductivity was ca 55-fold lower for the aerogel compared to the loose tubes, owing to a much larger necking index. Furthermore, the apparent electrical conductivity is key to efficient Pt utilization and ORR activity: the values of the kinetic current at 0.90 V vs. RHE decreased with decreasing apparent electrical conductivity of the SnO_2-based supports. The ORR specific/mass activity was four times higher on Pt/Nb-doped SnO_2 with loose tube structure relative to Pt/Nb-doped SnO_2 with aerogel structure. Based on these findings, electrospinning appears to be a promising route to synthesize Nb-doped SnO_2 supports for PEMFC electrocatalysts.

Acknowledgments The authors gratefully acknowledge Pierre Ilbizian for supercritical drying and Suzanne Jacomet for SEM observations of the TO and NTO aerogels.

Compliance with Ethical Standards

Funding The authors acknowledge financial support from the French National Research Agency through the SURICAT project (grant number ANR-12-PRGE-007) and the European Union's Seventh Framework Program for the Fuel Cells and Hydrogen Joint Technology Initiative under grant agreement No. 325239 (FCH-JU project Nano-CAT) as well as Capenergies and Tenerrdis. MC thanks the French IUF for its support. SC acknowledges the European Research Council under the European Union's Seventh Framework Programme (FP/2007 − 2013)/ERC Grant Agreement No. 306682.

Conflict of interest The authors declare that they have no conflict of interest (financial or non-financial).

References

1. A. Lamibrac, G. Maranzana, O. Lottin, J. Dillet, J. Mainka, S. Didierjean, A. Thomas, C. Moyne, J Power Sources **196**, 9451 (2011)
2. J. Durst, A. Lamibrac, F. Charlot, J. Dillet, L.F. Castanheira, G. Maranzana, L. Dubau, F. Maillard, M. Chatenet, O. Lottin, Appl Catal B Environ **138–139**, 416 (2013)
3. L. Dubau, L. Castanheira, F. Maillard, M. Chatenet, O. Lottin, G. Maranzana, J. Dillet, A. Lamibrac, J.-C. Perrin, E. Moukheiber, A. ElKaddouri, G. De Moor, C. Bas, L. Flandin, N. Caqué, Wiley Interdiscip Rev Energy Environ **3**, 540 (2014)
4. L. Castanheira, W.O. Silva, F.H.B. Lima, A. Crisci, L. Dubau, F. Maillard, ACS Catal **5**, 2184 (2015)
5. L. Castanheira, L. Dubau, M. Mermoux, G. Berthomé, N. Caqué, E. Rossinot, M. Chatenet, F. Maillard, ACS Catal **4**, 2258 (2014)
6. S. Maass, F. Finsterwalder, G. Frank, R. Hartmann, C. Merten, J Power Sources **176**, 444 (2008)
7. F. Maillard, A. Bonnefont, F. Micoud, Electrochem Commun **13**, 1109 (2011)
8. N. Linse, L. Gubler, G.G. Scherer, A. Wokaun, Electrochim Acta **56**, 7541 (2011)
9. L.M. Roen, C.H. Paik, T.D. Jarvi, Electrochem Solid-State Lett **7**, A19 (2004)
10. S.J. Tauster, S.C. Fung, R.L. Garten, J Am Chem Soc **100**, 170 (1978)
11. S.J. Tauster, S.C. Fung, Occur among Bin Oxides Groups IIA-VB **55**, 29 (1978)
12. S.J. Tauster, S.C. Fung, R.T.K. Baker, J.A. Horsley, Science **211**, 1121 (1981)
13. M.G. Sanchez, J.L. Gazquez, J Catal **104**, 120 (1987)
14. U. Diebold, Surf Sci Rep **48**, 53 (2003)
15. Q. Fu, T. Wagner, S. Olliges, H.D. Carstanjen, J Phys Chem B **109**, 944 (2005)
16. Q. Fu, T. Wagner, Surf Sci Rep **62**, 431 (2007)
17. F. Micoud, F. Maillard, A. Gourgaud, M. Chatenet, Electrochem Commun **11**, 651 (2009)
18. F. Micoud, F. Maillard, A. Bonnefont, N. Job, M. Chatenet, Phys Chem Chem Phys **5**, 1182–1193 (2010)
19. V.A. O'Shea, M.C.A. Galván, A.E.P. Prats, J.M. Campos-Martin, J.L.G. Fierro, Chem Commun (Camb) **47**, 7131 (2011)
20. G. Cognard, G. Ozouf, C. Beauger, G. Berthomé, D. Riassetto, L. Dubau, R. Chattot, M. Chatenet, F. Maillard, Appl Catal B Environ **201**, 381 (2017)
21. Y. Takabatake, Z. Noda, S.M. Lyth, A. Hayashi, K. Sasaki, Int J Hydrogen Energy **39**, 5074 (2014)
22. F. Takasaki, S. Matsuie, Y. Takabatake, Z. Noda, A. Hayashi, Y. Shiratori, K. Ito, K. Sasaki, J Electrochem Soc **158**, B1270 (2011)
23. Y. Senoo, K. Taniguchi, K. Kakinuma, M. Uchida, H. Uchida, S. Deki, M. Watanabe, Electrochem Commun **51**, 37 (2015)
24. A. Masao, S. Noda, F. Takasaki, K. Ito, K. Sasaki, Electrochem Solid-State Lett **12**, B119 (2009)
25. S. Cavaliere, S. Subianto, I. Savych, M. Tillard, D.J. Jones, J. Rozière, J Phys Chem C **117**, 18298 (2013)
26. E. Fabbri, A. Rabis, R. Kötz, T.J. Schmidt, Phys Chem Chem Phys **16**, 13672 (2014)
27. K. Kakinuma, Y. Chino, Y. Senoo, M. Uchida, T. Kamino, H. Uchida, S. Deki, M. Watanabe, Electrochim Acta **110**, 316 (2013)
28. Y. Senoo, K. Kakinuma, M. Uchida, H. Uchida, S. Deki, M. Watanabe, RSC Adv **4**, 32180 (2014)
29. J. Suffner, S. Kaserer, H. Hahn, C. Roth, F. Ettingshausen, Adv Energy Mater **1**, 648 (2011)
30. M. Sudan Saha, R. Li, M. Cai, X. Sun, Electrochem Solid-State Lett **10**, B130 (2007)
31. Y. Fan, J. Liu, H. Lu, P. Huang, D. Xu, Electrochim Acta **76**, 475 (2012)
32. H. Zhang, C. Hu, X. He, L. Hong, G. Du, Y. Zhang, J Power Sources **196**, 4499 (2011)
33. M. Dou, M. Hou, D. Liang, W. Lu, Z. Shao, B. Yi, Electrochim Acta **92**, 468 (2013)
34. G. Ozouf, C. Beauger, J Mater Sci **51**, 5305 (2016)
35. M. Batzill, U. Diebold, Prog Surf Sci **79**, 47 (2005)
36. C.A. Reiser, L. Bregoli, T.W. Patterson, J.S. Yi, J.D.L. Yang, M.L. Perry, T.D. Jarvi, Electrochem Solid State Lett **8**, A273 (2005)
37. L. Dubau, M. Lopez-Haro, L. Castanheira, J. Durst, M. Chatenet, P. Bayle-Guillemaud, L. Guétaz, N. Caqué, E. Rossinot, F. Maillard, Appl Catal B Environ **142–143**, 801 (2013)
38. L. Dubau, L. Castanheira, M. Chatenet, F. Maillard, J. Dillet, G. Maranzana, S. Abbou, O. Lottin, G. De Moor, A. El Kaddouri, C. Bas, L. Flandin, E. Rossinot, N. Caqué, Int J Hydrogen Energy **36**, 21902-21914 (2014)
39. L. Castanheira, L. Dubau, F. Maillard, Electrocatalysis **5**, 125 (2014)
40. L. Dubau, L. Castanheira, G. Berthomé, F. Maillard, Electrochim Acta **110**, 273 (2013)
41. Z. Zhao, L. Castanheira, L. Dubau, G. Berthomé, A. Crisci, F. Maillard, J Power Sources **230**, 236 (2013)
42. A.F. Mayadas, M. Shatzkes, Phys Rev B **1**, 1382 (1970)
43. Y. Wang, T. Brezesinski, M. Antonietti, B. Smarsly, ACS Nano **3**, 1373 (2009)
44. I. Savych, S. Subianto, Y. Nabil, S. Cavaliere, D. Jones, J. Rozière, Phys Chem Chem Phys **17**, 16970 (2015)
45. I. Savych, J. Bernard D'Arbigny, S. Subianto, S. Cavaliere, D.J. Jones, J. Rozière, J Power Sources **257**, 147 (2014)
46. L.J. Van der Pauw, Philips Res Reports **13**, 1 (1958)
47. S. Brunauer, P.H. Emmett, E. Teller, J Am Chem Soc **60**, 309 (1938)
48. S. Cavaliere, I. Jiménez-Morales, G. Ercolano, I. Savych, D. Jones, J. Rozière, Chem Electro Chem (2015). doi:10.1002/celc.201500330
49. J.F. Boyle, K.A. Jones, J Electron Mater **6**, 717 (1977)
50. C. Xu, J. Tamaki, N. Miura, N. Yamazoe, Sens Actuators, B **3**, 147 (1991)
51. C. Xu, J. Tamaki, N. Miura, N. Yamazoe, J Mater Sci **27**, 963 (1992)

52. A.B. Suryamas, G.M. Anilkumar, S. Sago, T. Ogi, K. Okuyama, Catal Commun **33**, 11 (2013)
53. D. Szczuko, J. Werner, S. Oswald, G. Behr, K. Wetzig, Appl Surf Sci **179**, 301 (2001)
54. D. Dobler, S. Oswald, J. Werner, W. Arabczyk, G. Behr, K. Wetzig, Chem Phys **286**, 375 (2003)
55. S. Oswald, G. Behr, D. Dobler, J. Werner, K. Wetzig, W. Arabczyk, Anal Bioanal Chem **378**, 411 (2004)
56. Y. Cross, D.R. Pyke, J Catal **58**, 61 (1979)
57. Y. Boudeville, F. Figueras, M. Forissier, J.L. Portefaix, J.C. Vedrine, J Catal **58**, 52 (1979)
58. E. Oakton, J. Tillier, G. Siddiqi, Z. Mickovic, O. Sereda, A. Fedorov, C. Copéret, New J Chem **40**, 2655 (2016)
59. M.A. Aegerter, Sol Energy Mater Sol Cells **68**, 401 (2001)
60. F. Maillard, P. Simonov, E.R. Savinova, in *Carbon Mater. Catal*, ed. by P. Serp, J.L. Figueiredo (John Wiley & Sons, Inc, New York, 2009), pp. 429–480